

A Sparse and Locally Coherent Morphable Face Model for Dense Semantic Correspondence Across Heterogeneous 3D Faces

Claudio Ferrari, *Member, IEEE*, Stefano Berretti, *Senior, IEEE*, Pietro Pala, *Senior, IEEE*, and Alberto Del Bimbo, *Senior, IEEE*

Abstract—The 3D Morphable Model (3DMM) is a powerful statistical tool for representing 3D face shapes. To build a 3DMM, a training set of scans in full point-to-point correspondence is required, and its modeling capabilities directly depend on the variability of the training data. Hence, to increase the descriptive power of a 3DMM, accurately establishing dense correspondence across heterogeneous scans with sufficient diversity in terms of identities, ethnicities, or expressions becomes essential. In this manuscript, we present a fully automatic approach that leverages a 3DMM to establish a dense correspondence across raw 3D faces. We propose a novel formulation to learn a set of sparse deformation components with local support on the face that, together with an original non-rigid deformation algorithm, allow the 3DMM to precisely fit unseen faces and transfer its semantic annotation to arbitrary 3D faces. We experimented our approach on three large and diverse datasets, showing it can effectively generalize to very different samples and accurately establish a dense correspondence even in presence of complex facial expressions. The accuracy of the dense registration is demonstrated by building a heterogeneous, large-scale 3DMM from more than 9,000 fully registered scans obtained by joining the three datasets.

Index Terms—3D Morphable Model, Sparse Components Learning, Dense Correspondence

1 INTRODUCTION

IN face analysis, one widely used statistical model that gained increasing interest throughout the years is the 3D Morphable Model (3DMM) [1]. Thanks to its ability to represent and manipulate 3D face shapes, it found successful application in a variety of tasks, spanning from single view reconstruction [2], [3], [4], computer graphics [5], to biometrics [6], [7], [8], [9] or medical imaging [10], [11], [12]. In general, a 3DMM can be constructed by computing an average face and a set of *deformation components*, learned from an ensemble of fully registered face scans (*i.e.*, scans having a point-to-point semantic correspondence). Irrespective of the method employed to learn the components, their capability of warping the average face and generate variegated novel faces depends on the variability of the training data. So, the availability of *heterogeneous* and *abundant* data results decisive to go a step further [13].

Heterogeneity can be achieved by including both inter-subject variability in terms of gender or ethnicity, and intra-subject changes due to pose, aging, expressions and topological variations (*e.g.*, mouth closed/mouth open). While for 2D images and videos the Web has been widely exploited as a natural source for collecting plentiful and variegated imagery, this is not the case for 3D data, which require dedicated and often expensive devices for acquisition. Consequently, the need for larger amounts of heterogeneous 3D data can be answered by resorting to the union of different datasets. However, acquisition devices used in dif-

ferent datasets are unlikely to share the same characteristics in terms of resolution or noise level, thus introducing an additional, unwanted level of variability. Further, while 2D image processing develops on the regular support given by the pixels grid, the irregular structure of 3D raw scans in terms of number and disposition of acquired points, demands for methods capable of establishing a dense, point-to-point correspondence.

A common way to establish such dense correspondence is that of relying on a *prior* in the form of a prototypical 3D face model (template). The template can be non-rigidly deformed and put in dense correspondence with each scan so that, transitively, the scans are in dense correspondence with each other. Despite the easy formulation, this is a challenging problem, where all the heterogeneity factors listed above come into play. An effective expedient consists in relying on the prior knowledge incorporated by a statistical face model, *i.e.*, the 3DMM, which can be leveraged to ensure statistically plausible deformations and regularize the process. Incidentally, we observe this is a *chicken-and-egg* problem, since such prior knowledge is learned from a training set of samples that need to be in dense correspondence. Therefore, to accurately adapt to novel face shapes, the capability of the 3DMM to apply deformations unseen in the training data becomes essential.

Overall, accurately solving the dense registration problem mainly depends on two factors: (i) The extent to which the learned components can capture the variability of the training data and generalize to unseen samples; (ii) How well the fitting process can maintain semantically meaningful associations between template and target. For both (i) and (ii), it has been shown that spatial locality is a desirable

• C. Ferrari, S. Berretti, P. Pala and A. Del Bimbo are with the Department of Information Engineering, University of Florence, Florence, Italy, 50139. E-mail: claudio.ferrari@unifi.it

Manuscript received ; revised.

property in contrast to 3DMMs that have global support on the face. On the one hand, it increases the model flexibility by decorrelating complex movements into local, separate deformations [14]; On the other, it can help to increase robustness to expressions and noise [15]. Still, this property is constrained by the variability of the training scans.

In this paper, we provide original solutions to the above points (i)-(ii); We propose a new method for learning localized yet anatomically meaningful deformation components that can widely generalize to unseen shapes, and a novel approach to establish dense semantic correspondence between a large variety of heterogeneous scans. We formulate the components learning by taking a complete new look at the training data, treating each vertex in the 3D faces, rather than each face model, as an independent sample. This allows us to extrapolate a larger spectrum of deformations, even from small training sets, while also reducing the impact of the correlation that exists between different points in the same face. Ultimately, this leads to improved generalization capabilities of the model. Our intuition comes from the observation that the fixed musculoskeletal structure induces neighboring vertices to move according to consistent patterns (principle of local consistency of motion), making it possible to approximate the movement of a local region with a single motion vector. We leverage this property by first learning a corpus of primary deformation directions from the aligned training scans, analyzing each vertex motion independently. Then, we learn how to expand each primary direction to a localized set of vertices by reconstructing the training samples using such primary directions. This is casted as a sparse-coding problem, which we solve using an Elastic-net formulation. We will show that with this formulation, the local consistency of motion ensures each direction is expanded and applied to neighboring points, allowing us to model sparse and localized deformations yet respecting the facial anatomy. The coefficients of the reconstruction constitute our *Sparse and Locally Coherent* (SLC) deformation components. Then, we design a solution that uses the learned components to deform the average model to target faces by means of an iterative optimization, named *Non-Rigid Fitting* (NRF). Its peculiarity consists in a novel strategy to establish the point-to-point correspondence between template and target, which assigns each vertex of the template to the centroid of its k -nearest neighbors in the target (Voronoi region). Together with an adaptive outliers rejection policy, it allows the template to smoothly adapt to large shape differences, *e.g.*, expressions, without requiring a sparse set of known landmarks for initialization, or to compute any surface descriptors. Finally, we transfer the semantic annotation from the deformed model to target faces putting them in dense correspondence.

In the experiments, we initially provide an ablation study that shows the proposed learning formulation allows building overcomplete representations that significantly increase the modeling generalization with respect to the standard PCA-based 3DMM in case of limited training sets. We then apply the proposed solutions for components learning and registration to the scans of the FRGCv2.0, Bosphorus and FaceWarehouse datasets, putting more than 9,000 diverse raw scans in dense correspondence. The accuracy of the registration is evaluated comparing with other model-

based state-of-the-art solutions in the task of landmark detection, and by building a *Heterogeneous Large-Scale* 3DMM from the registered scans of the three datasets, showing enhanced modeling capabilities as result of the large number and variety of samples.

In summary, the main contributions of this work are: (i) We propose a new solution to learn sparse and locally-consistent deformation components. Those augment the generalization capabilities of the model during fitting by disentangling complex facial movements, and can be used to apply face deformations in an intuitive way; (ii) We design a dense registration algorithm that can accurately fit the template to neutral as well as expressive scans, without requiring landmarks to initialize the deformation; (iii) We use the approaches in (i) and (ii) to establish dense correspondence between a large set of 3D face scans from heterogeneous datasets. We then show the registered scans are accurate enough to derive a 3DMM with largely improved modeling capabilities.

The rest of the paper is organized as follows: In Section 2, we summarize the works in the literature that are more close to our proposed solution; In Section 3, we formulate a new approach for learning localized deformation components of a 3DMM; The 3DMM is then included in a framework for dense semantic annotation transfer in Section 4; Extended experimental results are reported in Section 5; Finally, discussion and conclusions are sketched in Section 6.

2 RELATED WORK

Constructing a 3DMM requires two main operations: Establishing group-wise dense correspondence between a training set of facial scans; Performing some statistical analysis on the registered data to derive an average model and a set of deformation components. For a comprehensive survey on 3DMM techniques we refer to [16].

Dense Correspondence between 3D Face Scans – Determining a dense correspondence between 3D point clouds can be seen as a particular case of a rigid/non-rigid registration problem. State-of-the-art methods can be categorized according to the fact they: (i) Compute surface descriptors that can be used to define few landmarks of the face [17], [18], [19], [20], [21], perform region matching [22], [23], [24] or initialize a graph-matching procedure [25], [26]; (ii) Resolve for an objective function to find a mapping between fiducial points [27], [28], [29], or (iii) Use a 3D model of the face to transfer a dense semantic labeling. In the following, we focus on the latter category. An in depth discussion on the topic of shape correspondence can be found in [30], [31].

Several solutions used a 3D model of the face to transfer a set of reference labels to a set of unlabeled scans. For example, Paysan *et al.* [32] proposed a registration based on the Non-rigid Iterative Closest Point (NICEP) [27] algorithm. Since NICEP cannot handle large missing regions and topological variations, facial expressions were not accounted for in this case. Gilani *et al.* [33] proposed to evolve level set curves with adaptive geometric speed functions to automatically put in correspondence a large number of landmarks. The method was refined in [34], where a multi-linear algorithm was used to establish dense point-to-point correspondence over a population of 3D faces varying in

identity, facial expression and poses. To deal with facial expressions, the deformation process needs to be initialized with a set of landmarks, that are detected using a deep convolutional network. Gilani *et al.* [35] proposed an algorithm that is based on the subsequent refinement of automatically detected sparse correspondences on the outer boundary of 3D faces. However, only neutral and few mild expressive scans are put in dense correspondence. Fan *et al.* [36] proposed a *template* warping strategy to achieve semantic and topological correspondence. First, a face is chosen as a template and used to provide a global alignment with the target faces using the Go-ICP [37], [38] algorithm. Then, preliminary correspondence and deformation from the template to the target are alternated and iterated for a few times to obtain a correspondence result that guarantees semantic association. Despite this approach does not rely on a sparse set of landmarks for initialization, it does not account for facial expressions. Fan *et al.* [22] achieved dense correspondence by deforming a template face with locally rigid motions that are guided by sparse seed points. To account for facial expressions, the deformation is initialized using four landmarks on the mouth region that are manually labeled in the target scans. A different solution that is instead capable of computing point-to-point correspondence across expressive faces is the one of Salazar *et al.* [23], which is yet guided by a set of pre-detected landmarks.

Our solution differentiates from the above as it is capable of putting in dense correspondence neutral as well as strongly expressive scans without requiring a landmark based initialization, whereas this is a prerequisite for all the previous works dealing with expressive shapes. This is arguably a valuable property as accurately detecting landmarks on 3D faces is by itself a challenging problem. In addition, our strategy allows us to put in correspondence and join together scans collected with different devices, *i.e.*, from different datasets; Differently, none of the above solutions explicitly addressed this issue.

Constructing Statistical 3D Face Models – Two aspects have a major relevance in characterizing the different methods for 3DMM construction: (1) The human face variability captured by the training scans, which directly depends on their number, and heterogeneity; (2) The approach employed to learn the components. The former point is relevant as the standard 3DMM cannot replicate deformations that do not appear in the training data, *e.g.*, facial expressions [39]. The second point determines to what extent the 3DMM is able to capture the latent structure contained in the data and generalize to unseen samples. Most of the literature on 3DMM construction relies on the seminal work of Banz and Vetter [1], who first presented a complete solution to derive a 3DMM by transforming the shape and texture from a training set of 3D face scans into a vector space representation based on PCA, each face representing a training sample. This original 3DMM proposal was further refined into the Basel Face Model (BFM) by Paysan *et al.* [32]. A popular multi-linear 3D face model, called FaceWarehouse (FWH), that introduced expressive scans in the 3DMM training set was proposed by Cao *et al.* [40]. More recently, Li *et al.* [41] proposed FLAME, a powerful multi-linear PCA model composed of shape, expression blendshapes and pose parameters that are

learned separately from 4D sequences. The latter improves upon the FaceWarehouse model by using a larger number of training scans, demonstrating the advantage of abundance of data. Some later methods investigated different ways to learn the deformation components. Brunton *et al.* [15] defined a multi-linear model based on wavelet decomposition, and showed the advantage of learning localized and decorrelated components to deal with identity and expression variations in a 3D-3D fitting scenario. They also showed that by selecting proper masks, higher robustness to occlusions is also achieved with respect to a global model. Still, to fit expressive faces, the deformation needs to be initialized with a set of landmarks. In addition, it needs a devoted, non-standard deformation procedure. Another method that exposed the capability of modeling local and spatially uncorrelated deformations is the work by Lüthi *et al.* [14], who generalized the PCA-based statistical shape model using a Gaussian Process 3DMM. Whereas they also elaborated on the importance of de-correlating facial movements to achieve more flexibility, the learned local deformations did not fully respect the anatomical structure of the face. This made it difficult to directly apply them for generating realistic face instances. Somewhat along the same lines is the work by Neumann *et al.* [5], who proposed a sparse variant of PCA with additional local support constraints to achieve localized yet realistic deformations. However, those are learned on mesh sequences of single subjects, and used mainly for artistic and animation purposes. The Dictionary Learning-based 3DMM (DL-3DMM) presented in [39], instead, generalized the PCA model by learning a dictionary of deformation components, joining shape and expression variations into a single model. This is used to increase the modeling capabilities by removing the orthogonality constraint as imposed by PCA. This solution however cannot perform sparse local deformations.

Recently, several solutions have been presented that apply Deep Neural Networks (DNNs) to learn non-linear 3D face models. These methods can regress shape and texture parameters directly from an input photo [42], or UV maps [43]. Some solutions added the capability of modeling extreme expressions using convolutional mesh autoencoders [44], [45]. Liu *et al.* [46] learned a non-linear face model from a huge set of raw 3D scans. They used the PointNet architecture [47] to convert point clouds to identity and expression latent representations, while also establishing a dense point-to-point correspondence among them. Incidentally, this is the unique method in the literature that exhibits the capability of dealing with scans from different databases. The training data also included synthetic scans for which a dense correspondence is known, so resembling a semi-supervised setup. Further, employing the PointNet architecture resulted in a global shape model.

The distinguishing trait of our solution with respect to the above is that in our formulation, vertices of the training scans are independent samples; So, the number of training samples is fixed, while the number of training scans defines the dimensionality of each sample. We will show this is advantageous to extrapolate more patterns from the data, increasing the modeling capabilities. Operating this way, we also reduce the impact of the correlation between regions of the same face, allowing us to jointly learn identity

and expression local deformations in a single model, yet ensuring realistic and interpretable deformations.

Large Scale Morphable Models – There are just few examples of MMs constructed on large and heterogeneous datasets. The first 3DMM constructed on a large set of training examples was presented by Booth *et al.* [13], [28]. They introduced a MM construction pipeline to derive their Large Scale Facial Model (LSFM) from 9,663 distinct facial identities (about 12,000 scans in total), including variations in age, gender and ethnicity. All the scans were acquired in neutral expression from the same device, and the dense registration relied on a set of labeled landmarks. Ploumpis *et al.* [48] presented a general approach to combine 3DMMs from different parts of an object class into a single 3DMM. They fused the variability and facial detail of the LSFM with the full head modelling of the Liverpool-York Head Model (LYHM) [49], thus creating the Combined Face & Head Model (CFHM). This provides a solution to the problem of combining existing models built using different templates that can only partly overlap, have different representation capabilities and are constructed from different datasets. Finally, the work of Ploumpis *et al.* [50] presented a complete model of the human head extending the previous ones by combining them with eyes and ears model.

All the above works resulted in models with remarkable and promising modeling capabilities, demonstrating the advantage of learning a 3DMM from a large and variegated set of scans. On the other hand, collecting and processing the data required a huge effort. In addition, handling expressive scans still represents a difficulty; In fact, all those large scale models do not deal with facial expressions, which evidently limits their potential. We argue our proposed work can be of great help in bridging this gap by providing a solution that allows combining together scans with a large spectrum of variabilities, including expressions, coming from datasets that have been already collected.

3 LEARNING SPARSE AND LOCALLY COHERENT DEFORMATION COMPONENTS

The work in [1] first presented a complete solution to derive a 3DMM by transforming the shape and texture from a training set of 3D faces into a vector space representation based on PCA. The idea is that of generating novel 3D faces s by deforming an average model \mathbf{m} through a combination of deformation components \mathbf{c}_i learned from the data:

$$\mathbf{s} = \mathbf{m} + \sum_{i=1}^k \mathbf{c}_i \alpha_i . \quad (1)$$

Although several alternatives to PCA have been later proposed to learn the components \mathbf{c}_i , the founding concept is that they should capture relevant relationships in the data, representing specific characteristics or attributes of faces. These can either be related to structural aspects that define the *identity* characteristics, *e.g.*, nose shape, femininity/masculinity, *etc.*; Otherwise, they can involve deformations of the movable face parts, *e.g.*, mouth opening/closing, muscular movements, *etc.*, which are independent from the identity, and are associated to facial *expressions*. In both the cases, the capability of generalizing to unseen deformations

depends on both the information carried by training faces, and the approach employed to learn the components \mathbf{c}_i .

In this work, we aim at deriving a set of deformation components that (i) model both identity and expression variations as defined above, (ii) are spatially localized and, (iii) are in compliance with the anatomical structure of the face. For this purpose, we developed a method to learn localized but meaningful deformations based on a sparse decomposition of the training matrix. To ensure we can jointly model identity and expression variations, we used as training data the registered models of the BU-3DFE dataset derived in [39].

3.1 Problem Formulation

Throughout this section, we assume the 3D faces are in full correspondence. We represent the geometry of a generic 3D face as a vector $\mathbf{f}_i = [x_1, y_1, z_1, \dots, x_m, y_m, z_m]^T \in \mathbb{R}^{3m}$ that contains the linearized (x, y, z) coordinates of the m vertices. Let $\mathbf{F} = [\mathbf{f}_1, \dots, \mathbf{f}_N] \in \mathbb{R}^{3m \times N}$ be the matrix of the N training scans, each with m vertices arranged column-wise. Our goal is to extract from \mathbf{F} a set of sparse deformation components. To this aim, we first compute the difference between training scans and the average 3D face:

$$\mathbf{m} = \frac{1}{N} \sum_{i=1}^N \mathbf{f}_i , \quad \mathbf{v}_i = \mathbf{f}_i - \mathbf{m} , \quad \forall \mathbf{f}_i \in \mathbf{F} . \quad (2)$$

Each \mathbf{v}_i represents the *displacement field* that transforms the average model \mathbf{m} into a training model \mathbf{f}_i . Such \mathbf{v}_i are then stacked to form a new matrix $\mathbf{V} = [\mathbf{v}_1, \dots, \mathbf{v}_N] \in \mathbb{R}^{3m \times N}$.

In the literature, approaches that were proposed to build a MM, such as [1], [39], [52], [53], [54], [55], all interpret each 3D face as a training sample, *i.e.*, a data point lying on a $3m$ -dimensional manifold. Operating this way, the components estimation is heavily influenced by the number of available scans; In addition, correlations between different parts of the same face are captured while learning the components.

We are interested in learning a set of sparse deformation components in which the interactions between different face parts can be decorrelated, yet ensuring plausible shape deformations respecting the facial anatomy. Recalling the principle of local consistency of motion, our intuition is that it is possible to approximate the motion of a set of local vertices with single, *primary directions*, and reproduce the deformation of arbitrarily small face regions by learning how to expand each primary direction to a set of vertices. To address this, we change the way we look at the training data: Instead of using each scan \mathbf{v}_i as a separate training sample as we would normally do, we treat each vertex coordinate as an independent sample. More precisely, the displacements of each coordinate across the N scans are used as training samples; So, each sample becomes an N -dimensional data point $\mathbf{v}'_i \in \mathbb{R}^N$ representing the statistics of variation each vertex coordinate is subject to, for a total of $3m$ training samples. The primary directions are extrapolated from the independent coordinate variations; then, we learn how to map each direction back to the $3m$ coordinates so as to deform the 3D model. The estimation of the primary directions and expansion coefficients is formulated as a sparse-coding problem, in which the goal is to find a set of directions that can be sparsely combined to reconstruct the training data.

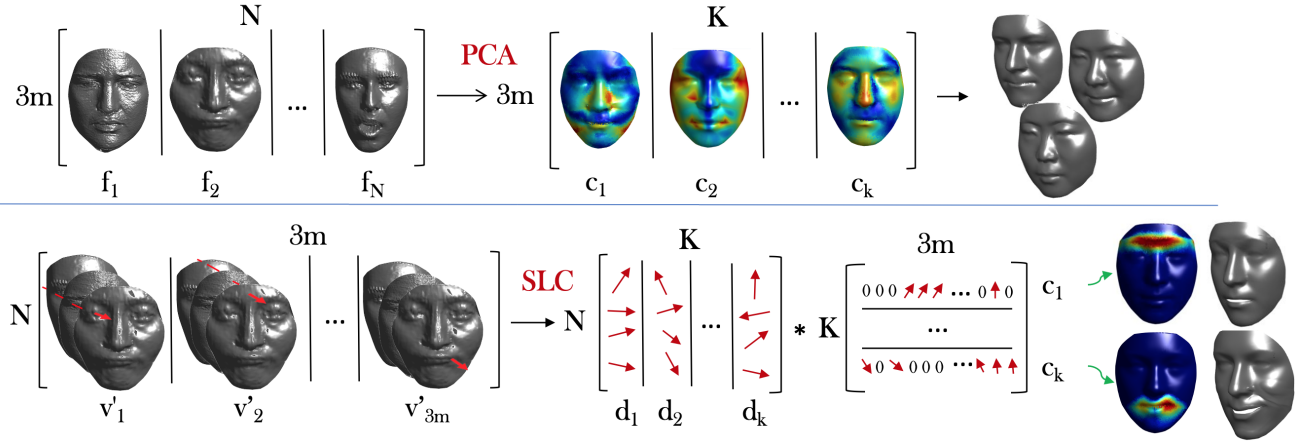


Fig. 1. Previous learning solutions, e.g., PCA [51] and others, interpret each 3D face as a training sample, and learn a set of $k < N$ deformation components (top row). In our solution (bottom row), we analyze each of the $3m$ displacements of the vertex coordinates \mathbf{v}'_i independently; A set of $k \ll 3m$ primary displacement directions \mathbf{d}_i is extracted from \mathbf{V}' ; The sparse coefficients \mathbf{c}_i identify a way to map the k learned directions back to all the $3m$ coordinates, and translate them into sparse deformation components.

3.2 Building the SLC-3DMM

Let $\mathbf{V}' = \mathbf{V}^T \in \mathbb{R}^{N \times 3m}$ be the transposed training matrix, so that each sample is $\mathbf{v}'_i \in \mathbb{R}^N$. We wish to find a set of k ($k \ll 3m$) primary directions $\mathbf{D} \in \mathbb{R}^{N \times k}$ and sparse expansion coefficients $\mathbf{C} = [\mathbf{c}_1, \dots, \mathbf{c}_{3m}] \in \mathbb{R}^{k \times 3m}$ that allow optimally reconstructing the input data, *i.e.*, such that $\|\mathbf{V}' - \mathbf{DC}\|_2^2$ is minimized and \mathbf{C} is sparse. To obtain realistic deformations, the coefficients should also be smooth, so to prevent discontinuities. We formulate the problem as:

$$\min_{\mathbf{c}, \mathbf{D}} \frac{1}{3m} \sum_{i=1}^{3m} \left(\|\mathbf{v}'_i - \mathbf{D}\mathbf{c}_i\|_2^2 + \lambda_1 \|\mathbf{c}_i\|_1 + \lambda_2 \|\mathbf{c}_i\|_2^2 \right). \quad (3)$$

This formulation is known as Elastic-net regression, which has some properties that make it particularly suitable for our task. The ℓ_1 penalty forces sparsity to the solution, while the ℓ_2 regularization encourages the *grouping effect* [56]. The latter occurs when the coefficients of a regression method associated to highly correlated variables tend to be equal. In our case, this correlation is in terms of displacement direction, and is caused by the local consistency of motion induced by facial muscles. The variables \mathbf{v}'_i , other than highly correlated, are hence highly spatially clustered as well. Exploiting this particular property, the learned \mathbf{c}_i will then contain similar values that are in turn spatially grouped. The two terms also interact with each other, contributing to the definition of the deformations extent.

Each of the k row vectors of \mathbf{C} expands the primary directions \mathbf{d}_i , which do not have a direct mapping to the $3m$ vertex coordinates, to a sparse, spatially bounded subset of the model vertices, ultimately letting us reproduce localized face deformations. The learning process is illustrated in Figure 1. Moreover, we observe that the displacement fields \mathbf{v}_i can include both positive or negative directions across the N models, e.g., a nose might be shorter or longer than the average one. To avoid \mathbf{D} and \mathbf{C} , in addition to learn the vertex motions, also introduce unwanted redundancy, we force a positivity constraint, which induces additional sparsity to the solution by promoting the complementarity of each learned atom [57]. Opposite directions can be even-

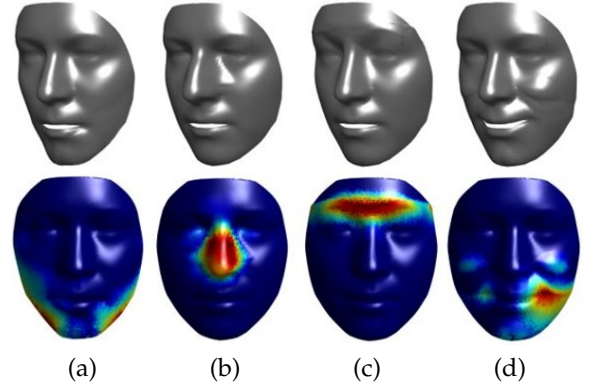


Fig. 2. Examples of learned components \mathbf{C} modeling structural traits related to the identity (a-b) as well as expressions (c-d).

tually reproduced by multiplication for a negative value. Further, each displacement field likely contains opposite directions occurring simultaneously in different facial regions, e.g., as for the “Angry” expression, where to a raising of the upper lip, a corresponding lowering of the eyebrows is observed. The positivity constraint allows decoupling such movements, which would not be compensated by the grouping effect alone. To summarize, (3) becomes:

$$\min_{\mathbf{c}, \mathbf{D}} \frac{1}{3m} \sum_{i=1}^{3m} \left(\|\mathbf{v}'_i - \mathbf{D}\mathbf{c}_i\|_2^2 + \lambda_1 \|\mathbf{c}_i\|_1 + \lambda_2 \|\mathbf{c}_i\|_2^2 \right), \quad (4)$$

s.t. $\mathbf{D} \geq 0, \mathbf{C} \geq 0$.

To solve (4), we exploit the implementation in [58] that alternates the estimation of \mathbf{D} and \mathbf{C} , while keeping the other fixed. We chose this particular implementation for its efficiency and versatility (please refer to [58] for more details). After convergence, we use the coefficients of the reconstruction \mathbf{C} as deformation components. Examples of the learned components are shown in Figure 2; Note how identity (e.g. nose shape, jawbone) and expression (e.g. smiling, eyebrow raising) deformations are independently reproduced and do not influence each other.

Finally, we observe that different facial regions can be more or less variable with respect to the average. Movable face parts surely present a higher degree of variability compared to the forehead, and this gets reflected in the magnitude of the elements of \mathbf{D} . In order to account for this imbalance that could affect the model fitting, we compute the mean of the dictionary elements over the N models for each direction k_i , and define a weight vector $\boldsymbol{\mu} \in \mathbb{R}^k$ with elements $\mu_j = \frac{1}{N} \sum_{i=1}^N d_{i,j}$, $\forall j \in [1, \dots, k]$. This represents the mean over each column of \mathbf{D} , *i.e.*, the mean contribution of each direction. We will use the vector $\boldsymbol{\mu}$ to regularize the deformation of the 3DMM, balancing the contribution of each component as detailed in Section 4.1.2. The sparse components \mathbf{C} , the average model \mathbf{m} and the weight vector $\boldsymbol{\mu}$ constitute our *Sparse and Locally-Coherent* (SLC)-3DMM.

4 DENSE SEMANTIC ANNOTATION TRANSFER

In this section, we describe our approach to non-rigidly deform a 3DMM to fit a target scan, and transfer the dense semantic annotation. As standard pre-processing step, the average model \mathbf{m} and a generic target shape $\mathbf{t} \in \mathbb{R}^{h \times 3}$ need to be roughly aligned. We assume the target scans are coarsely facing the camera, so that the whole face surface is visible and the orientation is consistent to \mathbf{m} (the problem of occlusions and head rotations is discussed in the supplemental material). The target shapes are then cropped using a sphere of radius $r = 95mm$ with center at the nose tip (vertex with largest z value). The shapes are zero-centered by subtracting the mean and rigidly aligned to \mathbf{m} by first making the nose-tips coincident, then using ICP registration to account for slight 3D rotation and translation shifts. This operation is performed as an initialization step. Note that, differently from previous works, the deformation is not initialized by any set of landmarks, neither for neutral nor for expressive scans. In the following, for the clarity of notation, we will use \mathbf{s} to refer to the fitted 3DMM shape at the current iteration, *i.e.*, $\mathbf{s} \equiv \mathbf{m} \in \mathbb{R}^{m \times 3}$ at the beginning (see also (1)), and to the coarsely aligned point-cloud as $\hat{\mathbf{t}}$.

4.1 Non-rigid Fitting

In order to deform \mathbf{s} to accurately match $\hat{\mathbf{t}}$, a novel approach named Non-Rigid Fitting (NRF) is designed. To deform \mathbf{s} , a preliminary correspondence between points in $\hat{\mathbf{t}}$ and \mathbf{s} must be established. The standard solution, like in [35], [59], is that of mapping each point of \mathbf{s} to its nearest-neighbor (NN) in $\hat{\mathbf{t}}$, deforming \mathbf{s} , and repeating these two steps until convergence. However, when dealing with very diverse scans, some inconveniences might arise. In fact, in presence of facial expressions and unseen identities, the difference between \mathbf{s} and a target point-cloud can be significantly large. Therefore, the initial correspondence is likely to be far from optimal. In previous works, this is solved by resorting to pre-detected landmarks to initialize the deformation.

Pairing each vertex of \mathbf{s} to one in $\hat{\mathbf{t}}$ is the core of the whole process, as the 3DMM is deformed under the guidance of such point-to-point correspondence. To address the above problems, we formulated a joint mean-point association and iterative outliers rejection strategy. In the following, we describe each step along with its rationale. We

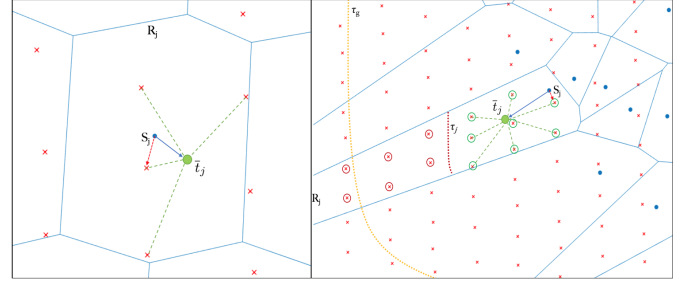


Fig. 3. Local Mean-Point association and outliers rejection. For each Voronoi region R_j (blue polygon) defined by \mathbf{s} , the point \mathbf{s}_j (blue dot) is associated to the centroid $\bar{\mathbf{t}}_j$ (green dot) of the points $\hat{\mathbf{t}}_{R_j}$ (red crosses). The local and global rejection thresholds (red and yellow dotted lines) are iteratively updated to progressively adapt to the global shape.

will show this solution leads to a significant improvement with respect to the standard one.

4.1.1 Local Mean Point Association

With the aim of selecting proper points to let the 3DMM adapt to any shapes, we sketched the point-to-point association strategy complying with the following observations:

- Multiple vertices $\hat{\mathbf{t}}_{R_j} = \{\hat{\mathbf{t}}_i, \dots, \hat{\mathbf{t}}_k\} \in \hat{\mathbf{t}}$ sharing a nearest-neighbor $\mathbf{s}_j \in \mathbf{s}$, belong to the Voronoi region R_j defined by \mathbf{s}_j ;
- Low curvature regions can be approximated with piecewise-planar surfaces;
- For high curvature regions, the closest point scheme might not reflect the local surface properties [60];
- Scanners usually induce high-frequency noise that would be desirable to attenuate.

Based on the observations above, our point-to-point associations operates by mapping each vertex \mathbf{s}_j to the centroid $\bar{\mathbf{t}}_j$ of the vertices $\hat{\mathbf{t}}_{R_j} = \{\hat{\mathbf{t}}_i, \dots, \hat{\mathbf{t}}_k\}$ belonging to the Voronoi region R_j . The latter can contain either a single or no points.

A key problem when computing $\bar{\mathbf{t}}_j$ is that of handling possible outliers. To account for that, we estimate both a global and a local rejection thresholds. The global threshold τ_g is computed as $\tau_g = \bar{d} + \sigma_d$, where \bar{d} is the average NN-distance between \mathbf{s} and $\hat{\mathbf{t}}$, and σ_d is the standard deviation. Each local threshold τ_j is computed in the same way, but separately for each Voronoi region R_j . The centroids $\bar{\mathbf{t}}_j$ are then computed after global and local thresholding, and mapped at position j in the re-indexed model $\hat{\mathbf{t}}^c$. Figure 3 exemplifies the procedure. This strategy has the advantage of letting \mathbf{s} iteratively adapt to the global shape of $\hat{\mathbf{t}}$ by avoiding getting attached to the closest points, yet maintaining the geometrical properties of the surface. It also compensates high frequency noise to a great extent.

Each \mathbf{s}_j associated to empty Voronoi regions R_j has a missing mapping to $\hat{\mathbf{t}}$. The association is completed by computing, for each non-paired point of \mathbf{s} , the nearest-neighbor in $\hat{\mathbf{t}}$, and mapping its indices $idx_{\hat{\mathbf{t}}}$ to their corresponding locations $idx_{\mathbf{s}}$ in the re-indexed model $\hat{\mathbf{t}}^c$. At the end of the process, each point of \mathbf{s} is paired. This ensures the uniqueness of the association, leading to a model $\hat{\mathbf{t}}^c$ with the same semantic indexing of \mathbf{s} . The pseudo-code is summarized in Algorithm 1.

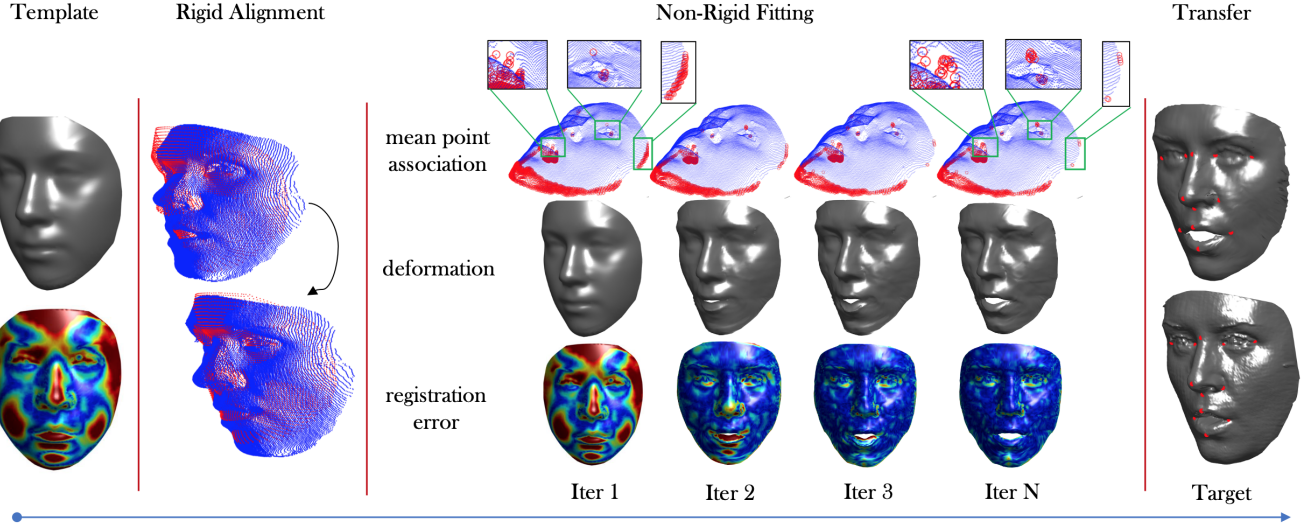


Fig. 4. Overview of the proposed pipeline for 3DMM fitting and dense semantic transfer. First, the template and target are rigidly aligned. Then, s is iteratively deformed guided by the proposed mean-point association for point-to-point correspondence estimation. Finally, the dense annotation of the 3DMM is transferred to the target. Red points denote the detected outliers, that are iteratively refined to let the template smoothly adapt to the target shape, while rejecting noisy local regions (e.g., points inside the mouth).

Algorithm 1: Point-to-Point Correspondence

Input: Deformed Model s , Target Shape \hat{t}
Output: Re-indexed Model \hat{t}^c

```

1  $\hat{t}^c = \text{ZerosLike}(s)$ ; // Initialize  $\hat{t}^c$ 
2  $\tau_g = \text{ComputeThreshold}(s, \hat{t})$ ;
/* Section 4.1.1 */
3 foreach  $s_j \in s$  do
4    $[R_j, \hat{t}_{R_j}] = \text{ComputePointsVoronoiRegion}(s_j, \hat{t})$ ;
5    $\tau_j = \text{ComputeThreshold}(s_j, \hat{t}_{R_j})$ ;
6    $\hat{t}_{R_j} = \text{RemoveOutliers}(\hat{t}_{R_j}, \tau_g, \tau_j)$ ;
7   if  $\hat{t}_{R_j} \neq \emptyset$  then
8      $\bar{t}_j = \text{ComputeCentroid}(\hat{t}_{R_j})$ ;
9      $\hat{t}^c(j) = \bar{t}_j$ ; // Assign  $\bar{t}_j$  to  $\hat{t}^c$  at index  $j$ 
10     $s = \text{RemoveVertices}(s, j)$ ; // Remove  $s_j$  from  $s$ 
11  $[idx_s, idx_{\hat{t}}] = \text{NNSearch}(s, \hat{t})$ 
12  $\hat{t}^c(idx_s) = \hat{t}(idx_{\hat{t}})$ ;

```

4.1.2 Model Deformation

The point-to-point correspondence from the previous step is exploited to refine the alignment of \hat{t}^c and s . This is useful prior to deforming s to account for slight scale differences and encourage an iterative refinement. To this aim, we estimate a similarity transformation:

$$s = \hat{t}^c \cdot \mathbf{P} + \mathbf{1} \cdot \mathbf{T}, \quad (5)$$

where $\mathbf{T} \in \mathbb{R}^{1 \times 3}$ is the 3D translation, $\mathbf{1} \in \mathbb{R}^{m \times 1}$ is the unitary vertical vector, and $\mathbf{P} \in \mathbb{R}^{3 \times 3}$ contains the 3D rotation and scale parameters. \mathbf{P} is found in closed-form solving the following least squares problem:

$$\arg \min_{\mathbf{P}} \|s - \hat{t}^c \cdot \mathbf{P}\|_2^2. \quad (6)$$

A solution to (6) is given by $\mathbf{P} = s^T \cdot (\hat{t}^c)^{\dagger}$, where \dagger indicates the pseudo-inverse. The translation is then recovered by aligning the barycenters, that is $\mathbf{T} = \bar{s} - \bar{\hat{t}^c} \cdot \mathbf{P}$. Using \mathbf{P} and \mathbf{T} , we re-align both \hat{t}^c and \hat{t} to s using Eq. (5) before performing the deformation.

Algorithm 2: Non-Rigid Fitting (NRF)

Input: Average Model m , Sparse Components C , Weights μ , Target Shape t , Error Threshold τ_e , Iterations Limit I_l
Output: Deformed Model s

```

1  $\hat{t} = \text{ICP}(t, m)$ ;
2  $err = \text{ComputeEuclideanError}(\hat{t}, m)$ ;
3  $s = m$ ,  $i = 0$ ,  $\delta_e = \tau_e + 1$ 
4 while  $i < I_l$  and  $\delta_e > \tau_e$  do
5    $\hat{t}^c = \text{P2PCorrespondence}(s, \hat{t})$ ; // Algorithm 1
6    $[\hat{t}^c, \hat{t}] = \text{SimilarityTransform}(\hat{t}^c, \hat{t}, s)$ ; // Eq. (5), (6)
7    $s = \text{SLCFitting}(\hat{t}^c, s, C, \mu)$ ; // Eq. (7), (8)
8    $e = \text{ComputeEuclideanError}(\hat{t}, s)$ ;
9    $\delta_e = err - e$ ;
10   $err = e$ ;
11   $i = i + 1$ ;

```

To deform s , we find the optimal set of deformation coefficients $\alpha \in \mathbb{R}^k$ so that the per-vertex distance between the two point sets is minimized. Similar to other works using a morphable model [35], [36], [39], we formulate the problem as a regularized least-squares:

$$\min_{\alpha} \|\hat{t}^c - s - C\alpha\|_2^2 + \lambda \|\alpha \circ \mu^{-1}\|_2, \quad (7)$$

where λ balances the contribution of the regularization term, which enforces smoothness to let the model approximate the target at small steps. Recalling the definition of μ in Section 3.2, we regularize the deformation using the inverse μ^{-1} so that the contribution of each component is weighed with respect to its average intensity. By pre-computing $\mathbf{X} = \hat{t}^c - s$, the solution is found in closed form:

$$\alpha = (C^T C + \lambda \cdot \text{diag}(\hat{\mu}^{-1}))^{-1} C^T \mathbf{X}, \quad (8)$$

where $\text{diag}(\hat{\mu}^{-1})$ denotes the diagonal matrix with vector $\hat{\mu}^{-1}$ on its diagonal. s is then deformed applying (1). Finally, we estimate the per-vertex error of the deformed model as the average Euclidean distance between each vertex of s and its nearest-neighbor in \hat{t} .

The NRF procedure is repeated until the error between subsequent iterations is above some threshold τ_e , or a maximum number of iterations is reached. The pipeline is sketched in Algorithm 2. The 3DMM is now fit to the target shape, and we can transfer the semantic labeling of s to \hat{t} .

4.2 Transfer the Semantic Annotation

To transfer the dense semantic annotation, each point of s must be associated to a distinct point in \hat{t} , so that the latter has the same semantic indexing of the morphable model. We again need to account for points of s sharing the same nearest-neighbor in \hat{t} . Addressing this issue allows obtaining a smoother mesh, where no vertices of s are collapsed into the same point. This is achieved by computing, for each vertex in s , its k -nearest neighbors in \hat{t} . If multiple points in s are mapped to the same point \hat{t}_k , the closest one is assigned to \hat{t}_k . The remaining are then mapped to the $(k-1)$ -nearest neighbors following the same scheme. The process ends when each point in s has been paired to a unique point in \hat{t} , leading to a re-indexed model \hat{t}' with the same semantic labeling of s . The pipeline is depicted in Figure 4.

5 EXPERIMENTAL RESULTS

Assessing the result of a dense correspondence algorithm is a complex task, since no solid definition of ground-truth exists. We carried out an extensive experimental validation to showcase the quality of our solution under different perspectives. We first investigate the effect induced by the individual components of our solution in an ablation study (Section 5.2). Following the standard practice, we then evaluate our approach in the task of 3D landmark correspondence, also in comparison with state-of-the-art solutions (Section 5.3). Finally, we use the densely registered scans to build a large-scale 3DMM, evaluate its performance (Section 5.4) and compare it against a model constructed from the BU-3DFE scans obtained from [39] (Section 5.5).

5.1 Datasets

In the experiments, we used three benchmarks that cover a wide range of different characteristics for 3D faces: the Face Recognition Grand Challenge (FRGCv2.0) [61], the Bosphorus [62], and the FaceWarehouse [63] datasets. A fourth dataset, the BU-3DFE [64], was used for training our morphable model. It comprises 100 subjects in neutral plus six expression, ranging from low to exaggerated intensity level.

FRGCv2.0 – It includes 4,007 scans of 466 individuals collected in two separate sessions. Approximately, 40% of the scans show slight spontaneous expressions. On average, the FRGCv2.0 scans have 35K vertices on the face region.

Bosphorus – This dataset comprises 4,666 high-resolution scans of 105 individuals. There are up to 54 scans per subject, which include prototypical expressions, facial action units activation, rotations and occlusions. Scans of Bosphorus have an average of 30K vertices on the face region. This dataset also contains rotated and occluded scans, that we did not use. In fact, in both the cases, the problem of dense correspondence is ambiguous. A qualitative and

quantitative evaluation on these subsets can be found in the supplemental material.

FaceWarehouse – This dataset comprises 3,000 Kinect RGB-D sequences of 150 individuals, aged 7-80. For each individual, 20 sequences are captured that include the neutral expression plus 19 natural expressions such as mouth-opening, smiling, kissing, etc. The data that have been released for public use consist of the first RGB-D frame of each sequence. The resolution of the point-clouds extracted from the depth frames is of about 15K vertices.

Parameter Settings – For all the reported experiments, the error threshold τ and the maximum number of iterations in Algorithm 2 have been set to 0.01 and 30, respectively. The regularization parameter λ in (8) was set to 1. The 3DMM used in this work has 6,704 vertices.

Computational Time – A Matlab implementation on a machine with Xeon CPU (2.6GHZ, single thread) has the following average computational times: ICP: 0.9s – Algorithm 1: 4.5s – Similarity Transform in (6): 0.01s – Deformation in (8): 0.02s – Annotation Transfer: 5.0s. Note that all the operations are highly parallelizable, and code optimizations can further reduce the computational times. The execution time of the complete pipeline depends on the number of NRF iterations, and can vary from $\approx 12s$ (1 iteration) to $\approx 140s$ (worst case scenario of 30 iterations). On average, 8-10 iterations are sufficient for convergence, taking approximately 40 seconds, against 100 and 160 seconds as reported, respectively, in [22] and [36], on a similar hardware. NICP [27] runs in approximately 70 seconds.

5.2 Ablation Study

In the following, we aim at delving into the details of the proposed learning approach (SLC) and registration algorithm (NRF). We will show that our novel components learning formulation leads to increased generalization capabilities with respect to previous solutions, mostly for smaller training sets containing limited variability. We then evaluate the fitting accuracy obtained by applying our NRF procedure (Algorithm 2) with various configurations of the SLC-3DMM, and analyze the impact of the learning parameters λ_1 , λ_2 , and k (Section 5.2.2).

5.2.1 SLC Learning

The major trait that differentiates the SLC solution with respect to previous 3DMM literature is the way in which we interpret the training data; Each training sample is a vector containing the displacement of each coordinate of each vertex across the N scans. Thus, independently from N , the number of training samples is fixed to $3m$. With this setup, we can build overcomplete representations, *i.e.*, with $k > N$, thus capturing a larger number of patterns in the data [65]. To showcase this advantage in the context of 3DMM construction, we learn the SLC-3DMM on a limited set of training samples. We divide the 1,779 fully registered scans of the BU-3DFE from [66] into train and test sets. The test set is composed of 10 male and 10 female random identities, for a total of 250 scans, comprising neutral as well as slight and strong expressions. From the remaining identities, we randomly sample 100 scans (with and w/o expressions) and use them to learn the SLC components with

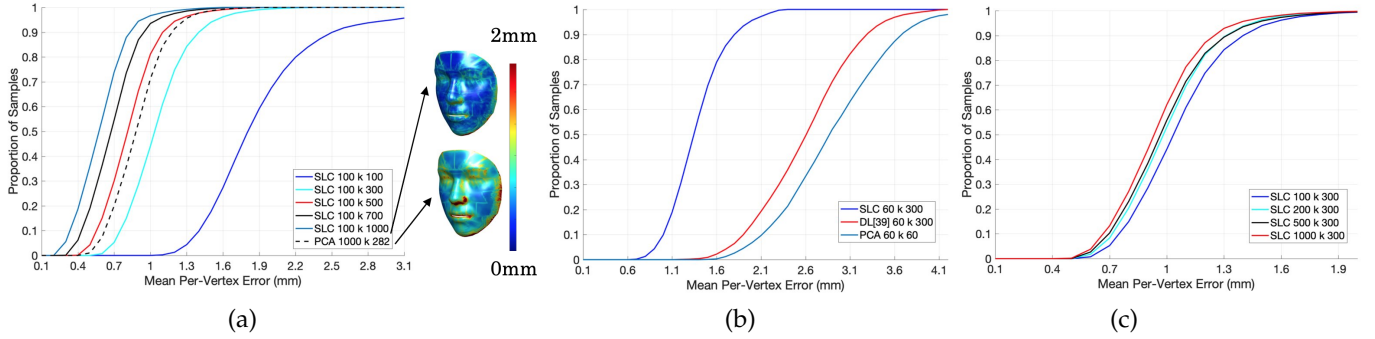


Fig. 5. Cumulative per-vertex error distribution comparing different configurations of the training set. Legends report “Method - # Training samples - # Components k ” (a) Generalization error varying the number of components. The error maps refer to a SLC trained on 100 scans with $k = 1000$ (top) and PCA model trained on 1,000 scans (bottom); (b) Generalization error training only on neutral scans; (c) SLC learned with different number of training samples ($k = 300$).

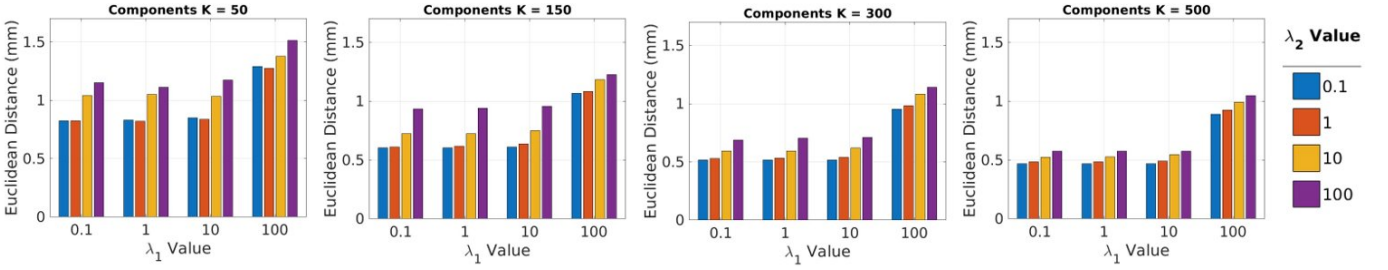


Fig. 6. Sensitivity analysis on the SLC parameters. Plots report the per-vertex error obtained on a sample of 200 scans from the FRGCv2.0 database applying Algorithm 2 with SLC components learned varying λ_1 and λ_2 . Each plot reports a different k .

varying k , from 100 to 1000 (overcomplete representation). For each shape in the test set, we estimate the deformation coefficients α using (8), and deform the average model using (1). Testing on scans in full correspondence with the template provides a faithful estimate of the fitting accuracy. The error is the mean per-vertex Euclidean distance.

Figure 5 (a) clearly shows that the generalization significantly improves by increasing k , even with a limited training set. Remarkably, using only 100 training scans, we can potentially surpass the generalization capability of a PCA model built from 1,000 scans (principal components retaining the 99% of the variance) by a large margin. This property is particularly valuable for generalizing to unseen shapes in case of smaller training sets with limited variability. This feature is particularly important for the task of accurate shape correspondence. The heatmaps also show that the error with SLC results generally lower but evenly distributed over the face. It is natural to question if this property still holds in case the 3DMM is learned only on neutral scans. Figure 5 (b) reports the fitting error obtained by a model learned using the subset of neutral scans (60 scans). The SLC-3DMM (with $k = 300$) achieves a significantly increased fitting precision with respect to both a PCA model (all the available principal components¹), and the DL-3DMM [39] (with $k = 300$). The test set includes neutral as well as expressive scans. The DL-3DMM is able to generalize better with respect to PCA, as reported in [39]; Even though k can be greater than the number of training samples N , in the DL setup the surplus components repre-

sent a redundant linear combination. Instead, our solution results in a powerful overcomplete representation. In this scenario, where the discrepancy between train and test sets is significant, the advantage of our formulation comes out evidently. However, in the most general case, we might want k to be small so as to keep the model compact. We thus investigate the effect of increasing the number of training samples. Results in Figure 5 (c) confirm that, when fixing the number of SLC components ($k = 300$), larger training sets result in enhanced fitting precision as expected.

5.2.2 SLC Parameters

As discussed in Section 3.2, λ_1 and λ_2 mainly define the spatial extent of each SLC component. The best choice of such parameters can follow two observations: (i) Each component needs to be sufficiently limited so that facial regions are deformed independently. This also maintains the founding concept of local consistency of motion; (ii) We still want the spatial extent to be large enough to cover the entire shape yet without introducing irregularities. Here, we explore the effect of learning parameters in a real fitting scenario. In Figure 6, we report the reconstruction error obtained by applying NRF (Algorithm 2) to a subset of 200 scans of the FRGCv2.0, using components learned with different values for λ_1 , λ_2 and k . The error is computed as the average per-vertex, nearest neighbor Euclidean distance between the fitted model s and \hat{t} . In this test, all the 1,779 training scans were used to build the SLC-3DMM. First, we note the per-vertex error is generally low and inversely proportional to k , consistently with the results of the previous section. Using all the available training scans,

1. In general, the maximum number of components is N .

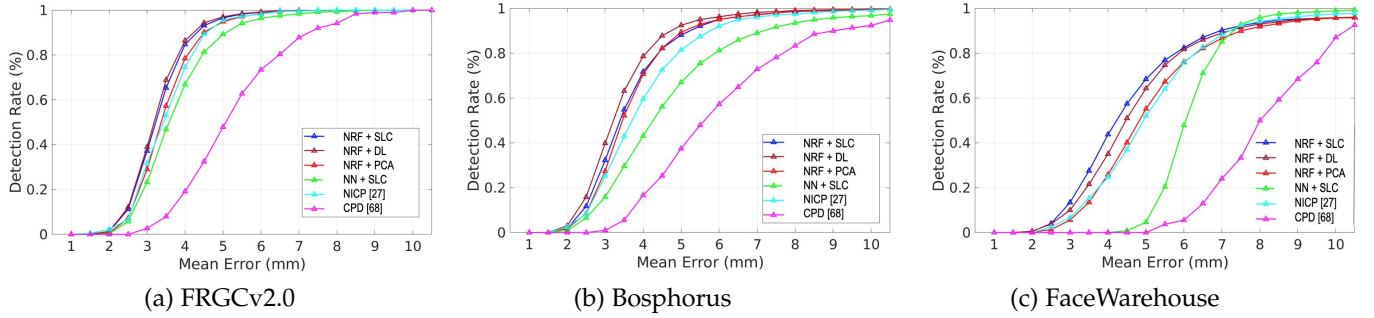


Fig. 7. Cumulative landmark localization error distributions for (a) FRGCv2.0, (b) Bosphorus, (c) FaceWarehouse.

even with as few as 50 components, the reconstruction error is yet reasonably low (less than 1mm). Parameters λ_1 and λ_2 , instead, behave consistently across different k . For each k , the highest per-vertex error is obtained when λ_2 is very large ($\lambda_2 = 100$), confirming that each component should be spatially bounded. The error decreases when the two parameters are balanced and kept stable to lower values (< 10), so that reasonably small regions are smoothly deformed. In fact, excessively large deformations (λ_2) imply undesired interactions, whereas smaller, non-smooth deformations (λ_1) can prevent the model capturing global shape variations. Despite more components increase the modeling diversity, which can be helpful to obtain accurate fittings, the non-negligible presence of noise in raw scans can impact on the smoothness of the result. Since our main goal is to densely register together a large number of heterogeneous scans, we privileged a configuration ensuring higher smoothness. So, unless otherwise stated, we employed a SLC configuration with $k = 50$, $\lambda_1 = 10$, and $\lambda_2 = 1$.

5.3 Landmarks Detection

In this section, we report a comparison between our dense registration method against standard techniques in a landmark detection task. Our proposal consists of a combination of a novel method for learning the 3DMM components (SLC) and a model fitting algorithm (NRF); Thus, we compare against methods falling in either one of the categories. First, to assess the contribution of the mean-point association, we substituted Algorithm 1 with the standard nearest-neighbor strategy for point-to-point correspondence. This solution is called NN+SLC in the following. Further, we compared against two standard non-rigid point-cloud matching techniques: the Coherent Point Drift (CPD) [68] and Non-Rigid ICP (NICP) [27]. Finally, we explored the behavior of the classic PCA-based 3DMM and the DL-3DMM in [39] when used in place of the proposed SLC, in conjunction with NRF. In the following, these two solutions are called, respectively, NRF+PCA and NRF+DL. For the PCA and DL variants, we chose the best configurations as reported in [39], where a detailed analysis was conducted. To evaluate the error, we first manually labeled a landmark configuration on the average model \mathbf{m} , obtaining a set of indices L_{idx} . The error is computed between the ground-truth annotations in $\hat{\mathbf{t}}$ provided by [17], [63], and our transferred landmarks obtained applying the full pipeline, *i.e.*, $\hat{\mathbf{t}}'(L_{idx})$.

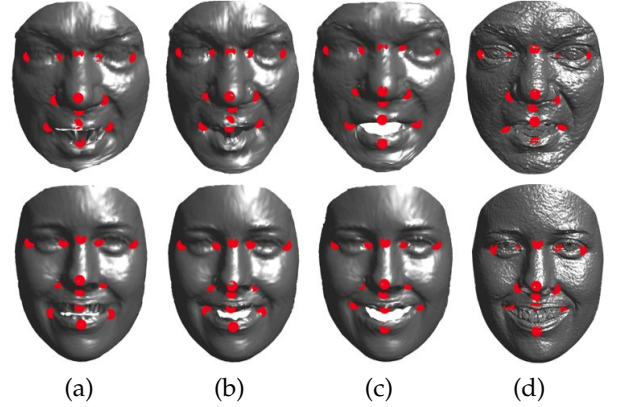


Fig. 8. Re-indexed models \mathbf{t}' with transferred landmarks $\mathbf{t}'(L_{idx})$ obtained using NICP [27] (a), the standard Nearest-Neighbor (b), and our proposed mean point association (c). The ground-truth scans are shown in (d). Our solution maintains a semantic consistency in case of large expressions and noise, especially in the mouth region.

Plots in Figure 7, show that the proposed mean-point association strategy, independently of the adopted components, leads to a more accurate landmark localization with respect to the standard nearest-neighbor (NN+SLC). Consistently with the literature, NICP provides competitive performance on FRGCv2.0, but struggles when more complex expressions are considered, as in Bosphorus or FaceWarehouse. The CPD algorithm performs badly in all the cases. The proposed mean-point association results advantageous especially for large shape differences, or when scans are characterized by a certain amount of noise. A qualitative example is depicted in Figure 8. Our solution demonstrated decisive for maintaining a semantic consistency in these cases, especially in the mouth region when it is wide open, exposing information such as the teeth. Some examples of fitted shapes \mathbf{s} are instead reported in Figure 9; Despite the presence of different noise sources (*e.g.*, beard, scanner noise) and large expressions, our algorithm results in smooth yet accurate fittings, without initializing the deformation with pre-detected landmarks.

Finally, we evaluate the NRF algorithm when used in conjunction with different 3DMM components, and show all the three approaches attain pretty accurate detections. When dealing with non-standard facial movements as those contained in FaceWarehouse though, the SLC-3DMM performs best, underlying the improved generalization to complex and unseen expressions and resilience to high noise levels.

TABLE 1

FRGCv2.0: Landmark localization error (mm). **Ex/En**-outer/inner eye corner, **N**-nose bridge, **Prn**-nose-tip, **Sn**-nasal base, **Ac**-nose corner, **Ch**-mouth corner, **Ls/Li**-upper/lower lip. Landmarks for Ex-En-Ch-Ac have been averaged. Best results in bold, second best in italic.

Method	Ex	En	N	Prn	Sn	Ac	Ch	Ls	Li	Avg
Creusot <i>et al.</i> [17]	5.9 ± 3.1	4.3 ± 2.2	4.2 ± 2.1	3.4 ± 2.0	3.7 ± 3.1	4.8 ± 3.6	5.6 ± 3.5	4.2 ± 3.2	5.5 ± 3.3	4.6 ± 2.9
BFM [51]	2.5 ± 2.2	<i>2.7 ± 2.2</i>	3.2 ± 2.2	2.3 ± 2.0	3.8 ± 3.6	8.3 ± 2.9	2.6 ± 2.9	2.6 ± 2.2	3.8 ± 3.7	3.5 ± 2.7
Sukno <i>et al.</i> [67]	4.7 ± 2.7	3.6 ± 1.7	2.5 ± 1.6	2.3 ± 1.7	2.7 ± 1.1	2.6 ± 1.4	<i>3.9 ± 2.8</i>	3.3 ± 1.8	4.6 ± 3.4	3.3 ± 2.0
K3DM _{BU} [35]	2.5 ± 2.2	2.4 ± 1.9	2.8 ± 1.8	2.6 ± 1.6	3.6 ± 1.9	6.1 ± 2.7	4.2 ± 3.1	2.9 ± 3.4	4.6 ± 2.9	3.5 ± 2.2
NRF+PCA	4.0 ± 1.8	3.3 ± 1.4	<i>2.1 ± 1.6</i>	<i>1.9 ± 1.0</i>	1.4 ± 1.4	3.5 ± 1.2	4.5 ± 2.2	2.8 ± 1.4	3.6 ± 2.1	3.0 ± 1.6
NRF+DL [39]	3.9 ± 1.8	3.1 ± 1.3	<i>2.1 ± 1.6</i>	1.8 ± 1.0	1.4 ± 1.3	3.1 ± 1.1	4.1 ± 2.0	<i>2.7 ± 1.4</i>	3.5 ± 2.0	2.9 ± 1.6
NRF+SLC	<i>3.8 ± 1.8</i>	3.0 ± 1.3	1.8 ± 1.5	<i>1.9 ± 1.0</i>	<i>1.5 ± 1.5</i>	<i>2.9 ± 1.2</i>	4.2 ± 2.2	2.8 ± 1.5	<i>3.6 ± 2.1</i>	2.8 ± 2.1
Fan <i>et al.</i> [22]	2.1 ± 1.9	1.9 ± 1.0	2.4 ± 1.2	1.8 ± 1.2	1.8 ± 0.9	1.9 ± 0.9	2.8 ± 2.5	2.0 ± 2.2	4.3 ± 3.1	2.3 ± 1.5

Method of [22] uses a different setting, and so is not directly compared

TABLE 2

Bosphorus: Landmarks localization error (mm). **Ex/En**-outer/inner eye corner, **N**-nose bridge, **Prn**-nose-tip, **Sn**-nasal base, **Ac**-nose corner, **Ch**-mouth corner, **Ls/Li**-upper/lower lip. Landmarks for Ex-En-Ch-Ac have been averaged. Best results in bold, second best in italic.

Method	Ex	En	N	Prn	Sn	Ac	Ch	Ls	Li	Avg
Cruesot <i>et al.</i> [17]	5.2 ± *	4.6 ± *	6.3 ± *	4.5 ± *	15.2 ± *	4.1 ± *	6.0 ± *	6.5 ± *	6.5 ± *	6.3 ± *
BFM [51]	3.6 ± *	<i>2.7 ± *</i>	2.2 ± *	2.9 ± *	3.6 ± *	4.0 ± *	5.9 ± *	4.0 ± *	6.5 ± *	3.9 ± *
Sukno <i>et al.</i> [67]	5.1 ± *	2.8 ± *	2.2 ± *	2.3 ± *	2.8 ± *	<i>3.0 ± *</i>	6.1 ± *	5.3 ± *	5.3 ± *	4.3 ± *
K3DM _{BO} [35]	3.6 ± *	2.5 ± *	2.3 ± *	2.8 ± *	2.3 ± *	2.7 ± *	<i>4.9 ± *</i>	3.3 ± *	5.0 ± *	3.3 ± *
NRF+PCA	4.1 ± 2.2	3.0 ± 1.5	2.0 ± 1.2	2.1 ± 1.4	<i>1.8 ± 1.9</i>	3.8 ± 1.6	5.1 ± 2.8	3.3 ± 1.8	4.0 ± 3.0	3.2 ± 1.9
NRF+DL [39]	<i>3.8 ± 2.0</i>	<i>2.7 ± 1.4</i>	<i>1.7 ± 1.1</i>	2.1 ± 1.3	1.8 ± 1.7	3.4 ± 1.4	4.7 ± 2.6	2.9 ± 1.7	4.0 ± 3.1	3.0 ± 1.9
NRF+SLC	3.9 ± 2.2	2.9 ± 1.5	1.5 ± 1.0	<i>2.2 ± 1.4</i>	1.8 ± 1.7	<i>3.0 ± 1.5</i>	5.2 ± 3.2	<i>3.2 ± 2.0</i>	<i>4.6 ± 3.9</i>	<i>3.1 ± 1.9</i>

* Standard deviations are not reported separately for the “Expressions” subset of the dataset.

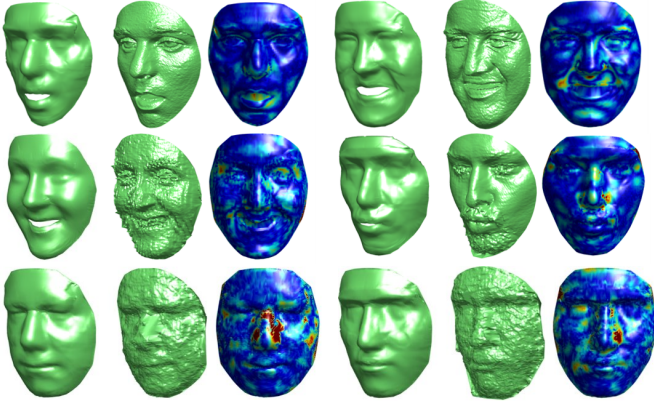


Fig. 9. Fitted shapes s (first, fourth columns) and the corresponding ground-truth faces (second, fifth columns). FRGCv2.0 (first row), Bosphorus (middle row) and FaceWarehouse (bottom row). The error heatmaps show the distribution of the per-vertex error.

5.3.1 Comparison with state-of-the-art

In this section, we compare our approach with model-based state-of-the-art works in terms of landmarks detection on the FRGCv2.0 and Bosphorus. We remark our approach was not specifically tailored for detecting landmarks; Though, it is relevant to assess to what extent it is accurate in such task as this represents a well established indicator of the dense registration accuracy. Results for the compared approaches have been collected from the original papers.

Table 1 reports results on the FRGCv2.0. Overall, our approach can localize landmarks with sufficient precision, performing better than other model-based approaches. Note that this represents a challenging cross-dataset scenario, as our SLC-3DMM is built from the registered scans of the BU-3DFE dataset. In this regard, Gilani *et al.* [35] built their K3DMs from different datasets; We report results of

the K3DM_{BU} which is built from the BU-3DFE for fair comparison. We also included the results obtained by Fan *et al.* [22]. It is relevant here to comment that in [22], in order to account for possible inaccurate manual labeling on the template, the algorithm was applied to the neighboring points of each specified landmark. Eventually, the detected landmark was replaced by the one with minimum error. Additionally, in case of expressions, they manually selected 4 landmarks around the mouth region, and used them to initialize the correspondence. Since these could represent a bias in the experiment, we report the result separately.

The advantage of our solution with respect to previous works comes out more evidently in Table 2, where results on Bosphorus are shown. For the compared approaches, we reported the results obtained for the “Expression” subset, consisting of 2,920 scans. Note that the largest improvement is obtained on the landmarks of the mouth region, especially the lower lip which, in case of examples with strong expressions, it is the one with largest variation. It is also worth noting that the K3DM_{BO} [35] model is built using scans of Bosphorus, whereas we perform a cross-database evaluation (results on this subset were not available for K3DM_{BU}).

We also report results on FaceWarehouse in Table 3. We cannot compare with other methods as, to the best of our knowledge, we are the first to perform 3D landmark detection on this dataset. Results are computed with respect to the landmark annotations provided therein. Similar to Figure 7, the NRF with all the three 3DMM solutions perform competitively. In this dataset though, point clouds are characterized by a high degree of noise, and also show particularly complex expressions. In such scenario, the advantage of our SLC turns out in a more evident way.

Qualitative landmark annotation transfer examples can be appreciated in Figure 10. We also report a few examples of re-indexed models with an extended set of transferred

TABLE 3

FaceWarehouse: Mean \pm Std of landmark localization error (mm). **Ex/En**-outer/inner eye corner, **Prn**-nose-tip, **Sn**-nasal base, **Ac**-nose corner, **Ch**-mouth corner, **Ls/Li**-upper/lower lip. Left and right landmarks for Ex-En-Ch-Ac have been averaged. Best results in bold

Method	Ex	En	Prn	Sn	Ac	Ch	Ls	Li	Avg
CPD [68]	6.8 \pm 3.2	5.3 \pm 2.7	3.4 \pm 1.5	6.4 \pm 4.1	8.8 \pm 4.7	14.1 \pm 5.4	6.6 \pm 3.2	9.6 \pm 3.8	7.6 \pm 3.6
NICP [27]	5.4 \pm 3.0	3.4 \pm 2.1	3.0 \pm 1.9	3.6 \pm 2.8	5.1 \pm 4.3	7.3 \pm 3.9	4.3 \pm 2.7	5.5 \pm 3.4	4.7 \pm 1.5
NRF+PCA	5.2 \pm 2.9	3.5 \pm 2.2	2.8 \pm 1.6	3.6 \pm 2.8	6.6 \pm 4.5	6.3 \pm 3.4	3.7 \pm 2.4	5.3 \pm 3.9	4.6 \pm 3.1
NRF+DL	5.1 \pm 2.8	3.0 \pm 1.9	2.6 \pm 1.6	3.5 \pm 2.7	6.1 \pm 4.5	5.8 \pm 3.2	3.4 \pm 2.4	5.0 \pm 3.9	4.3 \pm 2.9
NRF+SLC	4.0 \pm 2.4	2.7 \pm 1.7	2.8 \pm 1.7	3.4 \pm 2.6	5.5 \pm 4.5	5.9 \pm 3.5	3.5 \pm 2.4	5.6 \pm 4.6	4.1 \pm 2.8

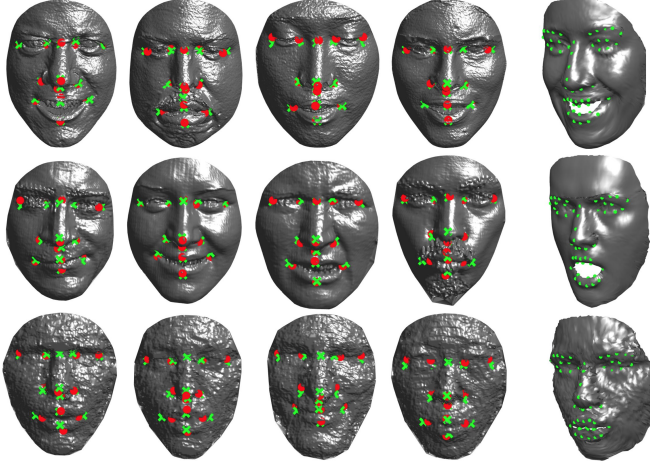


Fig. 10. Qualitative examples of landmark detection results on FRGCv2.0 (top row), Bosphorus (middle row), and FaceWarehouse (bottom row). Ground-truth annotations (red dots) and our transferred ones (green crosses) are plotted over the raw scans. Our approach is robust to different surfaces, noise, and topological changes. Some examples of re-indexed models \hat{t}' with an extended set of transferred landmarks are also shown (rightmost column).

landmarks, in order to highlight the capability of maintaining the semantic consistency in presence of large topological changes. Finally, we wish to remark that all the reported detections are obtained as a result of the dense registration process; Landmark detection is instead addressed independently in the compared works.

5.4 Heterogeneous Large-scale Morphable Model

We have exhaustively discussed that the more variability is contained in the training data, the more powerful and descriptive the morphable model. The capability of establishing dense correspondence between a large set of heterogeneous scans, possibly including complex non-standard expressions, is thus arguably beneficial for improving any statistical shape model, irrespective of the learning approach. The accuracy of the registration process results crucial for this purpose. In this section, we further verify the validity of the proposed dense registration by building a standard PCA model from the dense corresponded scans of FRGCv2.0, Bosphorus and FaceWarehouse, and evaluating its intrinsic characteristics. To compare the different algorithms and demonstrate the value of our proposal, we build four different models using, respectively, our proposed NRF in conjunction with SLC, PCA, and DL [39] deformation components, and the NICP, which is the standard solution employed in the vast majority of literature works [28], [50].

We considered all the available scans, for a total of 9,927 training samples, comprising 721 individuals with posed and spontaneous facial expressions, and a large variability in terms of age and ethnicity. To evaluate the intrinsic characteristics of this *Heterogeneous Large Scale Morphable Model* (HLS-3DMM), we follow a common practice in the literature of statistical shape models and use *compactness*, *generalization* and *specificity* measures [69]. We underline here that performing a direct comparison with other large-scale models is not possible because of the very different topology of the templates. In particular, the LSFm in [13] uses the BFM template [51] that includes the ears and the eyeballs; The Universal Head Model (UHM) in [50], includes the whole cranium, ears and eyes. In both these works, evaluations are reported with respect to a consistent template. For the sake of completeness, we will comment and discuss the outcomes with respect to that works, and compare with a PCA model built from the BU-3DFE scans of [39], which have the same topology of our template.

5.4.1 Compactness

Compactness measures the percentage of variance of the training data that is explained by a model when a certain number of principal components are retained, and follows the principle “*the less, the better*”. It mainly depends on two factors: (i) How precisely the dense registration algorithm maintained semantic consistency across the training samples; (ii) The variance contained in the training data, *i.e.*, number of identities, presence of expressions, etc. In Figure 11 (a), we report the plots of the HLS-3DMM, comparing the model constructed from the scans registered with the proposed method and NICP. The PCA bases derived using our registration algorithm result highly compact, with the SLC variant slightly outperforming PCA and DL. It explains more than 90% of the variance with as few as 43 principal components (47 with PCA and 58 with DL). This result is consistent with [53], where the same variance is retained with approximately 40 components. Being the number of training samples similar ($\approx 10,000$), the data in [53] contain around 9,000 identities collected from the same device, but no expressions. Our training set has 471 identities, but includes much more variability in terms of posed and natural facial expressions. The most relevant outcome though is that our models result much more compact with respect to NICP (90% of the variance needs 114 components), indicating the significantly increased accuracy of registration.

5.4.2 Generalization

Generalization measures the ability of the model to represent novel instances of face shapes that are unseen during train-

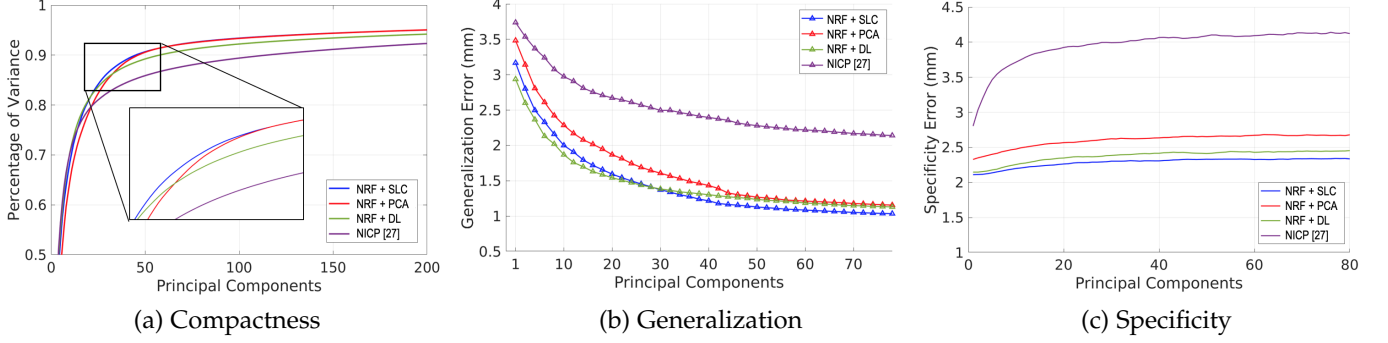


Fig. 11. Compactness, generalization and specificity measures for the HLS-3DMM constructed from 9,927 registered scans.

ing. To this aim, following the standard practice, we split the registered scans into a train and a test set. The test set is composed of 300 scans, chosen randomly and in equal proportion from the three datasets, *i.e.*, 100 from FRGCv2.0, 100 from Bosphorus and 100 from FaceWarehouse, to guarantee sufficient diversity. The remaining identities are used for training so that identities between train and test do not overlap. The different HLS-3DMMs are built applying PCA to the reduced training set. To compute the generalization error, for each shape in the test set, we estimate the deformation coefficients α using (8), and deform the average model using (1). The error is computed as the mean per-vertex Euclidean distance, and is shown in Figure 11 (b). We observe the capability of HLS-3DMM built using our solution to generalize well to unseen samples. The SLC variant performs better than the others from 30 components onward, suggesting more and variegate deformations were captured in the registration process. Other results in the recent literature report similar outcomes, with the UHM model in [50] having a generalization error ranging from 3 to 0.5mm, and the LSFm in [13] ranging from 1.8 to 0.3mm for neutral scans only. Again, we obtain a significant improvement with respect to a model resulting from NICP.

5.4.3 Specificity

Specificity evaluates the validity of synthetic faces generated by the model. We randomly generated 1,000 synthetic faces for a fixed number of principal components and measured how close they are from the samples in the test set. For each synthetic face, we found the sample in the test set with minimum error in terms of (average) per-vertex Euclidean distance. The curve in Figure 11 (c) reports the average of this error across all the synthetic faces. In comparison with other works, we attain good specificity error. For example, Booth *et al.* [13] reported errors varying from 1 to 1.8mm on a test set of neutral models only; Ploumpis *et al.* [50], instead, reported errors varying from 2.25 to 3.25mm for their UHM. Our model is capable of generating realistic faces, which also include facial expressions. As a desirable behavior, we observe the error remains stable even for a larger number of components. Our three models again outperform the NICP significantly.

5.5 Comparing with Previous Models

In this section, we showcase the increased modeling capability of the HLS-3DMM against a PCA model constructed

from the 1,779 registered scans of the BU-3DFE as obtained from [39]. To this aim, we use the same 300 scans composing the test set defined in Section 5.4.2, and compare the fitting accuracy of the two models. Without loss of generality, we perform the fitting and compute the error in the same way as in Section 5.4.2². For both, the number of principal components retaining the 99% of the variance are used. Figure 12 clearly shows the significantly improved accuracy with respect to the BU-3DFE model. This is attributed both to the larger training set used, and the accuracy of their dense registration: The significantly larger variability included allows it to generalize well to a wider variety of faces, even though the BU-3DFE already contained posed expressions in the training set.

5.6 Manipulating Registered Faces

Another common way to qualitatively assess the fidelity of a dense registration algorithm consists in manipulating the registered 3D faces. To this aim, we learn the SLC components as described in Section 3 from the 9,927 registered scans. Then, we deform some of them by applying randomly chosen SLC components (each deformation is obtained using a single component). In Figure 13, few examples are shown. We can observe that local areas are smoothly warped with realistic and natural deformations.

2. The comparison is possible as all the scans share the same topology.

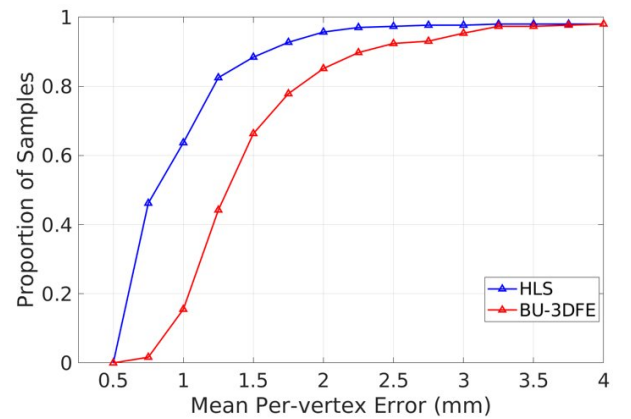


Fig. 12. Cumulative error distribution of the per-vertex fitting error between PCA models built from the newly registered 9,927 scans (HLS), and 1,779 scans of the BU-3DFE.

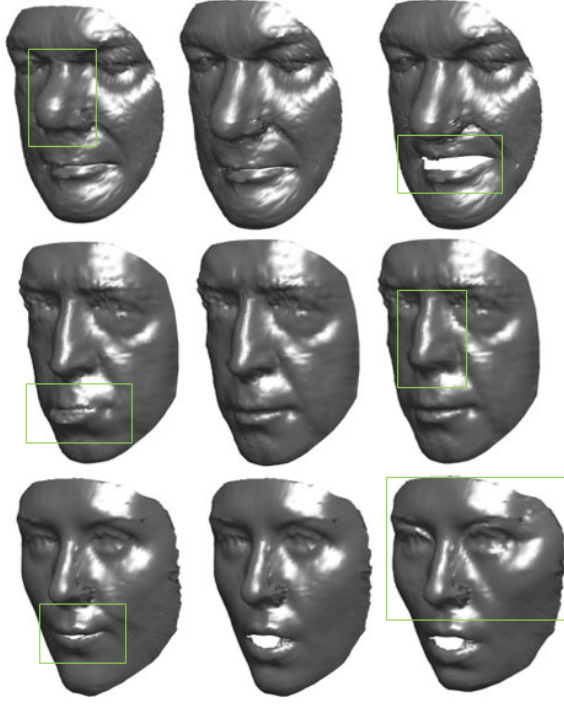


Fig. 13. Qualitative examples of local deformations applied to registered scans (middle column) by means of our SLC components. Each deformation is obtained using a single component.

This suggests semantic consistency was maintained during registration. In addition, the applied deformations result accurate even if applied to non-neutral scans (Figure 13, bottom row). Finally, we again note identity (nose shape, cheek size) as well as expression (mouth opening/closing) deformations can be performed.

6 CONCLUSIONS

In this paper, we proposed a dense 3D face correspondence approach, which leverages a 3DMM to transfer a point-to-point semantic annotation across raw 3D faces. We proposed a novel formulation to learn sparse and locally coherent deformation components that showed noteworthy generalization potential to new and unseen facial deformations. We showed that, by radically changing the interpretation of the training data and treating each vertex in the scans as independent samples, it is possible to learn sparse and decorrelated facial motions with high generalization potential. The model deformation is guided by the proposed Non-Rigid Fitting algorithm, specifically tailored for adapting to heterogeneous scans and large shape differences. The approach demonstrated to be accurate even in presence of strong facial expressions, and for very different types of 3D faces without the need of any landmark based guidance. We then densely registered together scans coming from three face databases, and demonstrated the value of our methods by building a large-scale, heterogeneous 3DMM from them, which exhibits remarkable modeling capabilities. The very different and complementary characteristics of the considered databases suggest the approach can be used to further enlarge the set of registered scans to, potentially, any database already collected.

REFERENCES

- [1] V. Blanz and T. Vetter, "A morphable model for the synthesis of 3D faces," in *ACM Conf. on Computer Graphics and Interactive Techniques*, 1999, pp. 187–194.
- [2] A. Tuan Tran, T. Hassner, I. Masi, E. Paz, Y. Nirkin, and G. Medioni, "Extreme 3D face reconstruction: Seeing through occlusions," in *IEEE Conf. on Computer Vision and Pattern Recognition (CVPR)*, 2018, pp. 3935–3944.
- [3] L. Galteri, C. Ferrari, G. Lisanti, S. Berretti, and A. Del Bimbo, "Deep 3D morphable model refinement via progressive growing of conditional generative adversarial networks," *Computer Vision and Image Understanding*, vol. 185, pp. 31–42, 2019.
- [4] B. Gecer, S. Ploumpis, I. Kotsia, and S. Zafeiriou, "Ganfit: Generative adversarial network fitting for high fidelity 3D face reconstruction," in *IEEE Conf. on Computer Vision and Pattern Recognition (CVPR)*, 2019, pp. 1155–1164.
- [5] T. Neumann, K. Varanasi, S. Wenger, M. Wacker, M. Magnor, and C. Theobalt, "Sparse localized deformation components," *ACM Trans. Graphics*, vol. 32, no. 6, pp. 179:1–179:10, 2013.
- [6] C. Ferrari, G. Lisanti, S. Berretti, and A. Del Bimbo, "Effective 3D based frontalization for unconstrained face recognition," in *Int. Conf. on Pattern Recognition*, 2016.
- [7] I. Masi, C. Ferrari, A. Del Bimbo, and G. Medioni, "Pose independent face recognition by localizing local binary patterns via deformation components," in *Int. Conf. on Pattern Recognition*, 2014.
- [8] J. Zhao, L. Xiong, J. Li, J. Xing, S. Yan, and J. Feng, "3d-aided dual-agent gans for unconstrained face recognition," *IEEE Trans. on Pattern Analysis and Machine Intelligence*, vol. 41, no. 10, pp. 2380–2394, 2018.
- [9] S. Ramanathan, A. Kassim, Y. V. Venkatesh, and W. S. Wah, "Human facial expression recognition using a 3D morphable model," in *Int. Conf. on Image Processing*, 2006.
- [10] B. Amberg, R. Knothe, and T. Vetter, "Expression invariant 3D face recognition with a morphable model," in *IEEE Int. Conf. on Automatic Face and Gesture Recognition*, 2008.
- [11] V. Blanz and T. Vetter, "Face recognition based on fitting a 3D morphable model," *IEEE Trans. on Pattern Analysis and Machine Intelligence*, vol. 25, no. 9, pp. 1063–1074, 2003.
- [12] X. Cao, Z. Chen, A. Chen, X. Chen, S. Li, and J. Yu, "Sparse photometric 3D face reconstruction guided by morphable models," in *IEEE/CVF Conf. on Computer Vision and Pattern Recognition (CVPR)*, 2018, pp. 4635–4644.
- [13] J. Booth, A. Roussos, A. Ponniah, D. Dunaway, and S. Zafeiriou, "Large scale 3D morphable models," *Int. Journal of Computer Vision*, vol. 126, no. 2, pp. 233–254, 2017.
- [14] M. Lüthi, T. Gerig, C. Jud, and T. Vetter, "Gaussian process morphable models," *IEEE Trans. on Pattern Analysis and Machine Intelligence*, vol. 40, no. 8, pp. 1860–1873, 2018.
- [15] A. Brunton, T. Bolkart, and S. Wuhler, "Multilinear wavelets: A statistical shape space for human faces," in *European Conf. on Computer Vision (ECCV)*. Springer, 2014, pp. 297–312.
- [16] B. Egger, W. A. P. Smith, A. Tewari, S. Wuhler, M. Zollhoefer, T. Beeler, F. Bernard, T. Bolkart, A. Kortylewski, S. Romdhani, C. Theobalt, V. Blanz, and T. Vetter, "3D morphable face models—past, present, and future," *ACM Trans. on Graphics*, vol. 39, no. 5, Jun. 2020.
- [17] C. Creusot, N. Pears, and J. Austin, "A machine-learning approach to keypoint detection and landmarking on 3D meshes," *Int. Journal of Computer Vision*, vol. 102, no. 1–3, pp. 146–179, 2013.
- [18] X. Lu and A. K. Jain, "Automatic feature extraction for multiview 3D face recognition," in *IEEE Int. Conf. on Automatic Face and Gesture Recognition (FGR)*, 2006, pp. 585–590.
- [19] M. Pamplona Segundo, L. Silva, O. R. P. Bellon, and C. C. Queirolo, "Automatic face segmentation and facial landmark detection in range images," *IEEE Trans. on Systems, Man, and Cybernetics, Part B (Cybernetics)*, vol. 40, no. 5, pp. 1319–1330, 2010.
- [20] P. Perakis, G. Passalis, T. Theoharis, and I. A. Kakadiaris, "3D facial landmark detection under large yaw and expression variations," *IEEE Trans. on Pattern Analysis and Machine Intelligence*, vol. 35, no. 7, pp. 1552–1564, 2013.
- [21] P. Perakis, T. Theoharis, and I. A. Kakadiaris, "Feature fusion for facial landmark detection," *Pattern Recognition*, vol. 47, no. 9, pp. 2783–2793, 2014.
- [22] Z. Fan, X. Hu, C. Chen, and S. Peng, "Boosting local shape matching for dense 3D face correspondence," in *IEEE/CVF Conf. on*

- Computer Vision and Pattern Recognition (CVPR)*, 2019, pp. 10936–10946.
- [23] A. Salazar, S. Wuhler, C. Shu, and F. Prieto, “Fully automatic expression-invariant face correspondence,” *Machine Vision and Applications*, vol. 25, no. 4, pp. 859–879, 2014.
- [24] Y. Sun and M. A. Abidi, “Surface matching by 3D point’s fingerprint,” in *IEEE Int. Conf. on Computer Vision (ICCV)*, vol. 2, 2001, pp. 263–269.
- [25] Y. Zeng, C. Wang, X. Gu, D. Samaras, and N. Paragios, “Higher-order graph principles towards non-rigid surface registration,” *IEEE Trans. on Pattern Analysis and Machine Intelligence*, vol. 38, no. 12, pp. 2416–2429, 2016.
- [26] Y. Zeng, C. Wang, Y. Wang, X. Gu, D. Samaras, and N. Paragios, “Dense non-rigid surface registration using high-order graph matching,” in *IEEE Conf. on Computer Vision and Pattern Recognition (CVPR)*, 2010, pp. 382–389.
- [27] B. Amberg, S. Romdhani, and T. Vetter, “Optimal step nonrigid ICP algorithms for surface registration,” in *IEEE Conf. on Computer Vision and Pattern Recognition (CVPR)*, 2007, pp. 1–8.
- [28] J. Booth, A. Roussos, S. Zafeiriou, A. Ponniah, and D. Dunaway, “A 3D morphable model learnt from 10,000 faces,” in *IEEE Conf. on Computer Vision and Pattern Recognition*, 2016, pp. 5543–5552.
- [29] H. Li, R. W. Sumner, and M. Pauly, “Global correspondence optimization for non-rigid registration of depth scans,” *Computer Graphics Forum*, vol. 27, no. 5, pp. 1421–1430, 2008.
- [30] B. Maiseli, Y. Gu, and H. Gao, “Recent developments and trends in point set registration methods,” *Journal of Visual Communication and Image Representation*, vol. 46, pp. 95–106, 2017.
- [31] G. K. L. Tam, Z. Cheng, Y. Lai, F. C. Langbein, Y. Liu, D. Marshall, R. R. Martin, X. Sun, and P. L. Rosin, “Registration of 3D point clouds and meshes: A survey from rigid to nonrigid,” *IEEE Trans. on Visualization and Computer Graphics*, vol. 19, no. 7, pp. 1199–1217, 2013.
- [32] P. Paysan, R. Knothe, B. Amberg, S. Romdhani, and T. Vetter, “A 3D face model for pose and illumination invariant face recognition,” in *IEEE Int. Conf. on Advanced Video and Signal Based Surveillance (AVSS)*, 2009, pp. 296–301.
- [33] S. Z. Gilani, F. Shafait, and A. Mian, “Shape-based automatic detection of a large number of 3D facial landmarks,” in *IEEE Conf. on Computer Vision and Pattern Recognition (CVPR)*, 2015, pp. 4639–4648.
- [34] S. Z. Gilani, A. Mian, and P. Eastwood, “Deep, dense and accurate 3D face correspondence for generating population specific deformable models,” *Pattern Recognition*, vol. 69, pp. 238–250, 2017.
- [35] S. Z. Gilani, A. Mian, F. Shafait, and I. Reid, “Dense 3D face correspondence,” *IEEE Trans. on Pattern Analysis and Machine Intelligence*, vol. 40, no. 7, pp. 1584–1598, 2018.
- [36] Z. Fan, X. Hu, C. Chen, and S. Peng, “Dense semantic and topological correspondence of 3D faces without landmarks,” in *European Conf. on Computer Vision (ECCV)*, vol. 11220, 2018, pp. 541–558.
- [37] J. Yang, H. Li, D. Campbell, and Y. Jia, “Go-icp: A globally optimal solution to 3D ICP point-set registration,” *IEEE Trans. on Pattern Analysis and Machine Intelligence*, vol. 38, no. 11, pp. 2241–2254, 2016.
- [38] J. Yang, H. Li, and Y. Jia, “Go-icp: Solving 3D registration efficiently and globally optimally,” in *IEEE Int. Conf. on Computer Vision*, 2013, pp. 1457–1464.
- [39] C. Ferrari, G. Lisanti, S. Berretti, and A. Del Bimbo, “A dictionary learning-based 3D morphable shape model,” *IEEE Trans. on Multimedia*, vol. 19, no. 12, pp. 2666–2679, 2017.
- [40] C. Cao, Y. Weng, S. Zhou, Y. Tong, and K. Zhou, “Facewarehouse: A 3D facial expression database for visual computing,” *IEEE Trans. on Visualization and Computer Graphics*, vol. 20, no. 3, pp. 413–425, 2014.
- [41] T. Li, T. Bolkart, M. J. Black, H. Li, and J. Romero, “Learning a model of facial shape and expression from 4D scans,” *ACM Trans. on Graphics (Proc. SIGGRAPH Asia)*, vol. 36, no. 6, pp. 194:1–194:17, 2017.
- [42] S. Sengupta, A. Kanazawa, C. D. Castillo, and D. W. Jacobs, “Sfsnet: Learning shape, reflectance and illuminance of faces in the wild,” in *IEEE Conf. on Computer Vision and Pattern Recognition (CVPR)*, 2018, pp. 6296–6305.
- [43] T. Bagautdinov, C. Wu, J. Saragih, P. Fua, and Y. Sheikh, “Modeling facial geometry using compositional vaes,” in *IEEE Conf. on Computer Vision and Pattern Recognition (CVPR)*, 2018, pp. 3877–3886.
- [44] A. Ranjan, T. Bolkart, S. Sanyal, and M. Black, “Generating 3D faces using convolutional mesh autoencoders,” in *European Conf. on Computer Vision (ECCV)*, vol. 11207, 2018, pp. 725–741.
- [45] Z.-H. Jiang, Q. Wu, K. Chen, and J. Zhang, “Disentangled representation learning for 3D face shape,” in *IEEE Conf. on Computer Vision and Pattern Recognition (CVPR)*, June 2019, pp. 11957–11966.
- [46] F. Liu, L. Tran, and X. Liu, “3D face modeling from diverse raw scan data,” in *IEEE/CVF Int. Conf. on Computer Vision (ICCV)*, 2019, pp. 9407–9417.
- [47] R. Q. Charles, H. Su, M. Kaichun, and L. J. Guibas, “Pointnet: Deep learning on point sets for 3D classification and segmentation,” in *IEEE Conf. on Computer Vision and Pattern Recognition (CVPR)*, 2017, pp. 77–85.
- [48] S. Ploumpis, H. Wang, N. Pears, W. A. Smith, and S. Zafeiriou, “Combining 3D morphable models: A large scale face-and-head model,” in *IEEE Conf. on Computer Vision and Pattern Recognition (CVPR)*, 2019, pp. 10934–10943.
- [49] H. Dai, N. Pears, W. Smith, and C. Duncan, “A 3D morphable model of craniofacial shape and texture variation,” in *IEEE Int. Conf. on Computer Vision (ICCV)*, 2017, pp. 3104–3112.
- [50] S. Ploumpis, E. Ververas, E. O’Sullivan, S. Moschoglou, H. Wang, N. Pears, W. Smith, B. Gecer, and S. P. Zafeiriou, “Towards a complete 3D morphable model of the human head,” *IEEE Trans. on Pattern Analysis and Machine Intelligence*, 2020.
- [51] P. Paysan, R. Knothe, B. Amberg, S. Romdhani, and T. Vetter, “A 3D face model for pose and illumination invariant face recognition,” in *IEEE Int. Conf. on Advanced Video and Signal Based Surveillance (AVSS)*, 2009, pp. 296–301.
- [52] P. Koppen, Z.-H. Feng, J. Kittler, M. Awais, W. Christmas, X.-J. Wu, and H.-F. Yin, “Gaussian mixture 3D morphable face model,” *Pattern Recognition*, vol. 74, pp. 617–628, 2018.
- [53] J. Booth, E. Antonakos, S. Ploumpis, G. Trigeorgis, Y. Panagakis, and S. Zafeiriou, “3D face morphable models ‘in-the-wild,’” in *IEEE Conf. on Computer Vision and Pattern Recognition (CVPR)*, 2017, pp. 5464–5473.
- [54] L. Tran and X. Liu, “Nonlinear 3D face morphable model,” in *IEEE Conf. on Computer Vision and Pattern Recognition (CVPR)*, 2018, pp. 7346–7355.
- [55] A. Brunton, A. Salazar, T. Bolkart, and S. Wuhler, “Review of statistical shape spaces for 3D data with comparative analysis for human faces,” *Computer Vision and Image Understanding*, vol. 128, no. 11, pp. 1–17, 2014.
- [56] H. Zou and T. Hastie, “Regularization and variable selection via the elastic net,” *Journal of the royal statistical society: series B (statistical methodology)*, vol. 67, no. 2, pp. 301–320, 2005.
- [57] J. Mairal, F. Bach, J. Ponce, and G. Sapiro, “Online learning for matrix factorization and sparse coding,” *Journal of Machine Learning Research*, vol. 11, pp. 19–60, 2010.
- [58] —, “Online dictionary learning for sparse coding,” in *Int. Conf. on Machine Learning*, 2009, pp. 689–696.
- [59] C. Ferrari, S. Berretti, P. Pala, and A. Del Bimbo, “3DMM for accurate reconstruction of depth data,” in *Int. Conf. on Image Analysis and Processing (ICIAP)*, 2019, pp. 532–543.
- [60] G. Pan, X. Zhang, Y. Wang, Z. Hu, X. Zheng, and Z. Wu, “Establishing point correspondence of 3D faces via sparse facial deformable model,” *IEEE Trans. on Image Processing*, vol. 22, no. 11, pp. 4170–4181, 2013.
- [61] P. J. Phillips, P. J. Flynn, T. Scruggs, K. W. Bowyer, J. Chang, K. Hoffman, J. Marques, J. Min, and W. Worek, “Overview of the face recognition grand challenge,” in *IEEE Work. on Face Recognition Grand Challenge Experiments*, Jun. 2005, pp. 947–954.
- [62] A. Savran, N. Alyüz, H. Dibekioğlu, O. Çeliktutan, B. Gökberk, B. Sankur, and L. Akarun, “Bosphorus database for 3D face analysis,” in *Proc. First COST 2101 Work. on Biometrics and Identity Management*, May 2008.
- [63] C. Cao, Y. Weng, S. Zhou, Y. Tong, and K. Zhou, “Facewarehouse: A 3D facial expression database for visual computing,” *IEEE Trans. on Visualization and Computer Graphics*, vol. 20, no. 3, pp. 413–425, 2013.
- [64] L. Yin, X. Wei, Y. Sun, J. Wang, and M. J. Rosato, “A 3D facial expression database for facial behavior research,” in *IEEE Int. Conf. on Automatic Face and Gesture Recognition (FG)*, 2006, pp. 211–216.
- [65] H. Lee, A. Battle, R. Raina, and A. Y. Ng, “Efficient sparse coding algorithms,” in *Advances in Neural Information Processing Systems (NIPS)*, 2007, pp. 801–808.
- [66] C. Ferrari, G. Lisanti, S. Berretti, and A. Del Bimbo, “Dictionary learning based 3D morphable model construction for face recogni-

tion with varying expression and pose,” in *Int. Conf. on 3D Vision*, 2015.

- [67] F. M. Sukno, J. L. Waddington, and P. F. Whelan, “3-d facial landmark localization with asymmetry patterns and shape regression from incomplete local features,” *IEEE Trans. on Cybernetics*, vol. 45, no. 9, pp. 1717–1730, 2014.
- [68] A. Myronenko and X. Song, “Point set registration: Coherent point drift,” *IEEE Trans. on Pattern Analysis and Machine Intelligence*, vol. 32, no. 12, pp. 2262–2275, 2010.
- [69] R. Davies, C. Twining, and C. Taylor, *Statistical models of shape: Optimisation and evaluation*. Springer Science & Business Media, 2008.



Claudio Ferrari received the Ph.D. in Information Engineering from the University of Florence in 2018. Currently, he is a postdoctoral researcher at the Media Integration and Communication Center (MICC) of the University of Florence. He has been a visiting research scholar at the University of Southern California (USC) in 2014. His research interests focus on computer vision and machine learning for biometrics and 2D/3D face analysis.



Stefano Berretti received the Ph.D. in Computer Engineering in 2001. Currently, he is an Associate Professor at University of Florence, Italy. He has been Visiting Professor at University of Lille and University of Alberta. His research interests focus on computer vision for face biometrics, human emotion and behavior understanding, computer graphics and multimedia. He is the Information Director and an Associate Editor of the ACM Transactions on Multimedia Computing, Communications, and Applications, and

Associate Editor of the IET Computer Vision journal.



Pietro Pala received the Ph.D. in Information and Telecommunications Engineering in 1997 at the University of Florence. Currently, he is Full Professor of Informatics Engineering at the School of Engineering of the University of Florence. His research activity focus on the use of pattern recognition models for multimedia information retrieval and biometrics, and on the study of 3D data for person and action recognition. He serves as editor for Multimedia Systems and ACM Transactions on Multimedia Computing, Communications, and Applications (TOMM).

Communications, and Applications (TOMM).



Alberto Del Bimbo is Full Professor of Computer Engineering at the University of Florence, Italy. His scientific interests include multimedia information retrieval, pattern recognition, image and video analysis and natural human–computer interaction. Prof. Del Bimbo is IAPR Fellow, Associate Editor of several leading journal in the area of pattern recognition and multimedia, and the Editor-in-Chief of the ACM Transactions on Multimedia Computing, Communications, and Applications. He was also the recipient of the

prestigious SIGMM 2016 Award for Outstanding Technical Contributions to Multimedia Computing, Communications and Applications.